First detection of AlF line emission towards M-type AGB stars

Citation for the original published paper (version of record):
Saberi, M., Khouri, T., Velilla Prieto, L. et al (2022). First detection of AlF line emission towards M-type AGB stars. Astronomy and Astrophysics, 663.
http://dx.doi.org/10.1051/0004-6361/202141704

A&A 663, A54 (2022)
https://doi.org/10.1051/0004-6361/202141704

Astronomy & Astrophysics

First detection of AlF line emission towards M-type AGB stars

M. Saberi[1,2], T. Khouri[3], L. Velilla-Prieto[3], J. P. Fonfría[4], W. H. T. Vlemmings[3], and S. Wedemeyer[1,2]

[1] Rosseland Centre for Solar Physics, University of Oslo, PO Box 1029 Blindern, 0315 Oslo, Norway
e-mail: `maryam.saberi@astro.uio.no`
[2] Institute of Theoretical Astrophysics, University of Oslo, PO Box 1029 Blindern, 0315 Oslo, Norway
[3] Dep. of Space, Earth and Environment, Chalmers University of Technology, Onsala Space Observatory, 43992 Onsala, Sweden
[4] Grupo de Astrofísica Molecular, Instituto de Física Fundamental, IFF-CSIC, C/Serrano, 123, 28006 Madrid, Spain

Received 2 July 2021 / Accepted 31 March 2022

ABSTRACT

The nucleosynthesis production of fluorine (F) is still a matter of debate. Asymptotic giant branch (AGB) stars are one of the main candidates for F production. However, their contribution to the total F budget is not fully known due to the lack of observations. In this paper, we report the detection of aluminium monofluoride (AlF) line emission, one of the two main carriers of F in the gas-phase in the outflow of evolved stars, towards five nearby oxygen-rich (M-type) AGB stars. We studied the Atacama large millimetre/submillimetre array (ALMA) observations of AlF (v = 0, J = 4–3, 9–8, 10–9, and 15–14) and (v = 1, J = 7–6) line emission towards o Ceti, and (v = 0, J = 7–6 and 15–14) lines towards R Leo. We also report a tentative detection of AlF (v = 0, J = 7–6) line in IK Tau, (v = 0, J = 15–14) line towards R Dor, and (v = 0, J = 7–6 and J = 15–14) lines in W Hya. From spatially resolved observations, we estimated the AlF emitting region with a radius $\sim 11 R_\star$ for o Ceti and $\sim 9 R_\star$ for R Leo. From population diagram analysis, we report the AlF column densities of $\sim 5.8\times10^{15}$ cm^{-2} and $\sim 3\times10^{15}$ cm^{-2} for o Ceti and R Leo, respectively, within these regions. For o Ceti, we used the C^{18}O (v = 0, J = 3–2) observations to estimate the H$_2$ column density of the emitting region. We found a fractional abundance of $f_{\mathrm{AlF/H_2}} \sim (2.5\pm1.7)\times10^{-8}$. This gives a lower limit on the F budget in o Ceti and is compatible with the solar F budget $f_{\mathrm{F/H_2}} = (5\pm2)\times10^{-8}$. For R Leo, a fractional abundance $f_{\mathrm{AlF/H_2}} = (1.2\pm0.5)\times10^{-8}$ is estimated. For other sources, we cannot precisely determine the emitting region based on the available data. Assuming an emitting region with a radius of $\sim 11 R_\star$ and the rotational temperatures derived for o Ceti and R Leo, we crudely approximated the AlF column density to be $\sim(1.2\text{–}1.5)\times10^{15}$ cm^{-2} in W Hya, $\sim(2.5\text{–}3.0)\times10^{14}$ cm^{-2} in R Dor, and $\sim(0.6\text{–}1.0)\times10^{16}$ cm^{-2} in IK Tau. These result in fractional abundances within a range of $f_{\mathrm{AlF/H_2}} \sim (0.1\text{–}4)\times10^{-8}$ in W Hya, R Dor, and IK Tau.

Key words. stars: abundances – stars: AGB and post-AGB – circumstellar matter

1. Introduction

Fluorine (F) is among the few elements whose cosmic origin is still the subject of debate. It has only one stable isotope (^{19}F), which can be easily destroyed by proton, neutron, and alpha particle capture reactions in stellar interiors (e.g. Ziurys et al. 1994; Abia et al. 2015). F is the most electronegative element, so it is extremely chemically reactive and can strongly bond to electron donors such as metals (Ziurys et al. 1994).

There are several scenarios to explain the cosmic F production: (i) He-burning shell flashes in asymptotic giant branch (AGB) stars with initial masses of ~2–4 $M_\odot$, subsequent thermal pulses, and third dredge-up; (ii) neutrino process occurring during supernova explosions; (iii) mergers between helium and carbon-oxygen white dwarfs; (iv) He-burning phase in Wolf–Rayet (WR) stars; (v) rapidly rotating massive stars (e.g. Woosley & Weaver 1995; Meynet & Arnould 2000; Karakas 2010; Longland et al. 2011; Abia et al. 2015; Jönsson et al. 2017; Limongi & Chieffi 2018; Ryde et al. 2020). A detailed overview of the F production sites and its role on the Galactic chemical evolution can be found in Grisoni et al. (2020, and references therein). The relative contributions of the aforementioned sites must be constrained by observations (e.g. Timmes et al. 1995; Spitoni et al. 2018; Olive & Vangioni 2019). Among all these candidates, AGB stars are the only sites of F production that have been observationally confirmed (Jorissen et al. 1992; Federman et al. 2005; Werner et al. 2005; Abia et al. 2015, 2019).

The AGB phase is a late phase of evolution for stars with an initial mass of 1–8 $M_\odot$. AGB stars play a significant role in the Galactic chemical evolution by ejecting of newly synthesised elements to the interstellar medium through strong stellar winds.

Models of Lugaro et al. (2004) and Karakas (2010) predict that the F enrichment is a strong function of the initial stellar mass and metallicity. For solar metallicity models, they predict the highest F formation in AGB stars with initial masses to be between 2 and 4 $M_\odot$ and for them to be maximal in the 3–3.5 $M_\odot$ mass range.

Jorissen et al. (1992) reported a fluorine over-abundance up to 30 times the solar value in AGB stars using the infrared vibration-rotation lines of hydrogen fluoride (HF). They also found that the fluorine enrichment is correlated with the enrichment of atomic carbon. An over-abundance ranging from 10–250 times the solar abundance are reported in a number of hot post-AGB stars from far-UV observations of F V and F IV (Werner et al. 2005). This significant over-abundance of F is believed to be the F synthesised during the preceding AGB phase, which is brought to the surface of the post-AGB star.

Previous determinations of F abundance in AGB stars are mainly based on near infrared observations of HF lines. However, significant contamination of these spectral lines with telluric lines in this wavelength region prevents accurate

Table 1. M-type AGB stars with detected AlF line emission.

Star	$\dot{M}$ $(10^{-7}\,M_\odot\,\mathrm{yr}^{-1})$	d (pc)	V_{LSR} (km s^{-1})	V_{exp} (km s^{-1})	$R_\star$ (mas)	$T_\star$ (K)	P (days)	$M_\star$ $(M_\odot)$
o Ceti	1	102	47	3	15	2800	332	1.0
R Leo	1	130	0.5	6	13.5	2800	310	1.5
W Hya	1	104	41	7	20	2950	388	1.0
R Dor	1	45	6.9	6	27.5	2400	175†	1.0–1.3
IK Tau	80	265	34	18.5	6	2100	470	1.1–1.5

Notes. Columns 2–8, for the first four sources, are taken from Vlemmings et al. (2019) and the stellar masses for W Hya, R Dor, and IK Tau are from Danilovich et al. (2017). For *o* Ceti and R Leo, they are estimated based on the ^{17}O/^{18}O ratio presented by De Nutte et al. (2017) and the O isotopic ratios are taken from Hinkle et al. (2016). For IK Tau, all parameters are taken from Velilla Prieto et al. (2017, and references therein). We note that $R_\star$ listed here are the measured radii in the near-infrared. †Period of R Dor varies between 175 and 362 days.

determination of the F abundance (e.g. Abia et al. 2009, 2010, 2015).

Chemical equilibrium models of F-bearing species predict a considerable amount of F to be locked into aluminium monofluoride (AlF) and HF in the outflow of AGB stars. The metal-containing molecules such as AlOF, CaF, and CaF$_2$ are also expected to be abundant at radii larger than 10$R_\star$ in M-type AGB stars (Agúndez et al. 2020). However, these species have not been detected in the outflow of AGB stars yet.

The lines of rotational transitions of AlF and HF have been previously reported in the outflow around the carbon-rich AGB star IRC+10216 (Ziurys et al. 1994; Agúndez et al. 2011, 2012). They estimated relative abundances of $f_{\mathrm{AlF/H_2}} \sim 1\times10^{-8}$ and $f_{\mathrm{HF/H_2}} \sim 8\times10^{-9,}$ which results in a lower limit of $f_{\mathrm{F/H_2}} \sim 2\times10^{-8}$ for the total F budget in IRC+10216. This is consistent with the solar value of $f_{\mathrm{AlF/H_2}} = (5\pm2)\times10^{-8}$ reported by Asplund et al. (2021). Moreover, Danilovich et al. (2021) recently reported the detection of rotational lines of AlF ($\upsilon = 0, J = 7$–6) towards the S-type AGB star, W Aql. They estimated a fractional abundance of $f_{\mathrm{AlF/H_2}} = 7.2\times10^{-8}$–$1.0\times10^{-7}$ in the inner CSE within a radius of $\sim$15 $R_\star$ and $f_{\mathrm{AlF/H_2}} = 4.0\times10^{-8}$ within $\sim$90$R_\star$ using radiative transfer modelling.

Observations of multiple transitions of F-bearing species at sub-millimetre wavelengths can provide a more accurate determination of the total F budget in AGB stars. In this paper, we report the first detection of rotational lines of AlF towards M-type AGB stars, *o* Ceti and R Leo, with the Atacama large millimetre/sub-millimetre array (ALMA). We also report tentative detection of AlF lines towards W Hya, R Dor, and IK Tau.

2. Observations

We used observations of the ALMA main arrays in Bands 4, 6, 7, and 8 from projects 2016.1.00004.S, 2017.1.00191.S, 2018.1.00749.S, and 2018.1.00649.S for *o* Ceti, projects 2016.1.01202.S and 2017.1.00862.S for R Leo, and project 2016.1.00119.S for IK Tau. In addition, we used ALMA compact array (ACA) observations in Band 8 from project 2018.1.01440.S for *o* Ceti, R Leo, R Dor, and W Hya and project 2016.2.00025.S for W Hya.

Table 1 lists the observed sources and their physical properties. The observed lines, their spectroscopic parameters, date of observations, and measured intensities are listed in Table 2. We also investigated any possible blends from the Cologne database for molecular spectroscopy (CDMS) (Müller et al. 2001, 2005) and jet propulsion laboratory (JPL) spectroscopic databases (Pickett et al. 1998) (see notes in Table 2).

The data calibration was performed following the standard ALMA procedures with the Common Astronomy Software Application (CASA) (McMullin et al. 2007). Details of the data processing can be found in Khouri et al. (2018); Vlemmings et al. (2019); Fonfría et al. (2019). The calibration uncertainty will depend on the flux calibrator used and typically ranges from 5 to 20% (Francis et al. 2020). In this paper, we assumed a typical 10% uncertainty for the flux calibration. The integrated flux uncertainties that are listed in column 7 in Table 2 include the uncertainties from flux calibration and from Gaussian fitting on the lines.

3. Excitation analysis and results

3.1. *o* Ceti

3.1.1. AlF population diagram

We identify four rotational lines of AlF within the ground vibrational state $\upsilon=0$, $J=4$–3, 9–8, 10–9, and 15–14, and the vibrationally excited line $\upsilon=1$, $J=7$–6, which are listed in Table 2. Rotational transition frequencies of AlF are taken from CDMS (Wyse et al. 1970; Hoeft et al. 1970). Figure 1 presents the integrated flux density of spatially resolved AlF lines towards *o* Ceti. From the $J=10$–9 line, the emitting region is estimated to have a diameter of $\sim$0.34″ $\sim$34 au $\sim$22 $R_\star$ based on the 3σ emission region, where $R_\star$ refers to the stellar radius measured in infrared.

We derived the column density of AlF towards these three regions: (1) the region with a diameter of $\sim$0.34″($\sim$22 $R_\star$) centred on the star shown in Fig. 1, rightmost panel, shown by a dotted-dashed white circle, encompassing all five observed AlF lines; (2) a circular region centred on the star with a diameter of 0.168″($\sim$11$R_\star$) shown in Fig. 1, rightmost panel, represented by a dotted magenta circle, where we use the three spatially resolved lines ($\upsilon=0$, $J=4$–3, 10–9, and $\upsilon=1$, $J=7$–6); (3) a small elliptical region at north–east of the star with a diameter of 0.055″ × 0.07″ ($\sim$4 $R_\star$) shown in Fig. 1, rightmost panel, represented by a dashed blue ellipse, where we could only use the AlF ($\upsilon=0$, $J=10$–9, and $\upsilon=1$, $J=7$–6) lines. The $\upsilon=0$, $J=4$–3 extracted from this region was too weak to be used for the analysis in region 3.

For regions 1 and 2, we used the population diagram method (Goldsmith & Langer 1999) to estimate the AlF rotational temperature (T_{rot}) and mean column density (N_{AlF}). This is a reasonable approximation since AlF lines are optically thin, as we show later, and AlF arises from a relatively small region ($<$11$R_\star$) in the inner part. Our analysis also shows that the rotational temperature does not vary significantly between regions 1 and 2. The rotational temperature describes the excitation of the rotational levels of the molecule, and in the case of local thermodynamic equilibrium (LTE), it also represents the kinetic temperature of the gas. For region 3, we were only able to use the $J=10$–9 line in the ground vibrational state, and a population diagram analysis was not possible.

The population level of a given molecule follows:

$$\ln\left(\frac{N_{\mathrm{u}}}{g_{\mathrm{u}}}\right) = \ln\left(\frac{N_{\mathrm{AlF}}}{Z}\right) - \frac{E_{\mathrm{u}}}{k_{\mathrm{B}}T_{\mathrm{exc}}}, \quad (1)$$

where N_{u} and g_{u} are the column density and statistical weight of the upper level, respectively, N_{AlF} is the total column density of the AlF molecules, Z is the partition function, E_{u} is the energy

Table 2. Detected AlF emission lines towards M-type AGB stars by ALMA observations.

Source	ν	Transition (GHz)	E_u	g_u (K)	A_{ul}	Flux ($10^{-3}\,s^{-1}$)	*FWHM* (Jy km s^{-1})	V_c (km s^{-1})	Ang. res. (km s^{-1})	M.R.S. (arcsec)	Apr. (arcsec)	Obs. date (arcsec)	ϕ
o Ceti	131.8988	υ = 0, J = 4–3	16	9	0.025	0.12 ± 0.04	5.9	47.8	0.077	2.897	0.25	21-09-17	0.9
	228.7165	υ = 1, J = 7–6	1184	15	0.147	0.46 ± 0.14	9.7	48.5	0.049	1.267	0.5	22-09-17	0.9
	296.6988	υ = 0, J = 9–8	71	19	0.299	1.84 ± 0.23	6.6	47.7	0.286	9.238	0.5	19-11-18	0.1
	329.6416 $^{(*)}$	υ = 0, J = 10–9	87	21	0.412	4.39 ± 0.59	8.7	47.2	0.022	0.570	0.5	09-11-17	0.8
	494.2268	υ = 0, J = 15–14	190	31	1.41	7.60 ± 0.84	6.2	47.4	0.172	11.962	0.5	28-11-18	0.1
R Leo	230.7938	υ = 0, J = 7–6	44	15	0.138	0.24 ± 0.06	7.2	–1.0	0.133	1.941	1	01-10-16	0.5
						0.26 ± 0.04	6.4	0.3	1.275	13.166	5	22-03-17	0.6
						0.22 ± 0.03	5.8	0.2	0.365	5.521	2	03-05-17	0.0
						0.15 ± 0.04	6.2	–2.3	0.028	0.695	0.3	21-09-17	0.7
						0.24 ± 0.05	4.3	–0.6	0.022	0.431	0.3	03-10-17	0.7
						0.19 ± 0.05	5.7	–0.6	0.025	0.597	0.3	27-10-17	0.9
	494.2268	υ = 0, J = 15–14	190	31	1.41	3.16 ± 0.49	5.7	0	2.570	15.118	CP	24-03-19	0.2
W Hya	230.7938 $^{(**)}$	υ = 0, J = 7–6	44	15	0.138	0.49 ± 0.15	11	39.0	5.089	29.537	CP	21-05-17	0.5
	494.2268	υ = 0, J = 15–14	190	31	1.41	4.29 ± 1.22	7.3	41.1	2.039	13.634	CP	08-06-19	0.8
R Dor	494.2268	υ = 0, J = 15–14	190	31	1.41	2.13 ± 0.72	7.7	5.5	2.135	13.812	CP	08-06-19	0.3
IK Tau	230.7938 $^{(**)}$	υ = 0, J = 7–6	44	15	0.138	0.23 ± 0.04	13.7	36.0	0.752	8.412	3	13-04-17	–

Notes. Spectroscopic data are taken from the CDMS. Integrated flux, the full width at half maximum (FWHM), and the line central velocity (V_c) are from Gaussian fitting. Flux uncertainties ($\sigma_{\rm Flux}$) are a summation of Gaussian fitting uncertainty and 10% of the total flux due to calibration uncertainty of ALMA data. MRS stands for maximum recoverable scale. Apr. denotes circular aperture used to extract the spectra, and CP denotes where the spectra are extracted from the central pixel (6.6″ × 4.4″) for the ACA observations. ϕ denotes the stellar variability phase at visual wavelengths where $\phi_{\rm min}$ = 1 and $\phi_{\rm max}$ = 0. $^{(*)}$ and $^{(**)}$ lines are likely blended with an SO_2 line at 329.6459 GHz and a $^{50}TiO_2$ line at 230.7931 GHz, respectively.

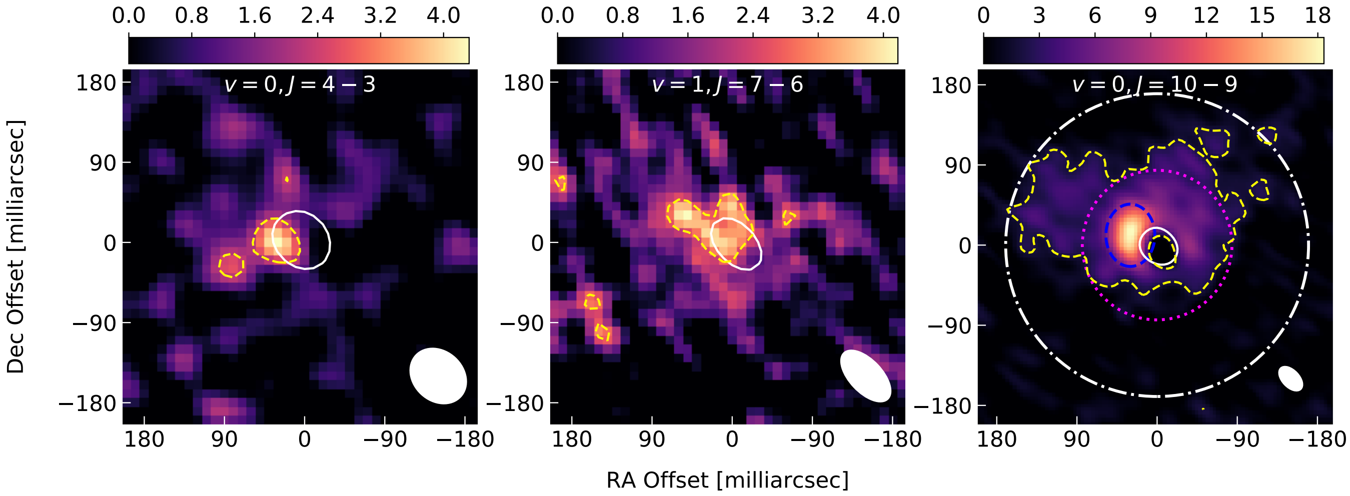

Fig. 1. Integrated emission of the spatially resolved lines of AlF towards *o* Ceti. The lines are integrated in the 131.873–131.883 GHz (41–54 km s^{-1}) range for the $\upsilon = 0$, $J = 4$–3 line, 228.675–228.685 GHz (36–59 km s^{-1}) for $\upsilon = 1$, $J = 7$–6, and 329.606–329.577 GHz (32–59 km s^{-1}) for the $\upsilon = 0$, $J = 10$–9 line. The scale is given in Jy km s^{-1} beam^{-1}. The lines shown are indicated at the top of each panel. The white contours show the 50% stellar continuum emission level at the corresponding frequencies and the dashed yellow contours mark the 3-σ level of the line emission. The filled white ellipses indicate the beam size in each observation. In the right panel, the regions over which the lines were integrated (see text) are indicated by the dashed blue ellipse (peak AlF emission), dotted magenta circle (CO υ = 1, J = 3–2 line emission region), and dotted-dashed white circle (all AlF emission lines).

of the upper level, k_B is the Boltzmann constant, and $T_{\rm exc}$ is the excitation temperature.

We assumed optically thin emission in the calculation of N_u, which is estimated using

$$N_u = \left(\frac{4\pi d^2}{\pi r_e^2}\right)\left(\frac{W}{A_{ul} h\nu}\right), \tag{2}$$

where the first term accounts for the geometrical dilution in which d is the distance to the source and r_e is the radius of the emitting region. W is the flux of the line in units (W m^{-2}), and for each line it is individually extracted from the regions that are listed above. A_{ul} represents the Einstein-A coefficients, which express the probability of the spontaneous emission from the upper level u to the lower level l.

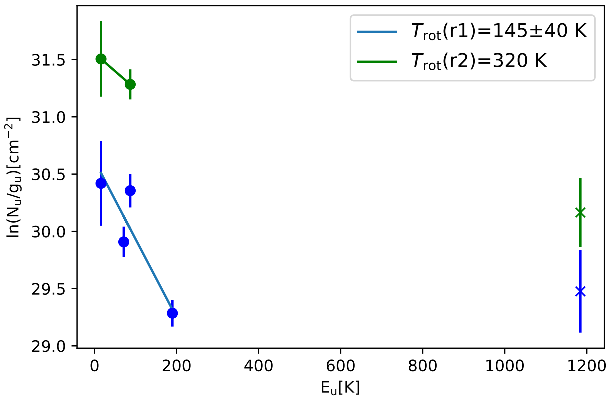

Fig. 2. Population diagram of observed AlF rotational transitions towards *o* Ceti that are listed in Table 2. Blue points correspond to flux densities that are extracted from region 1 and green points correspond to those from region 2 (see Sect. 3.1 for explanations). The vibrationally excited $v = 1$ lines in both regions are also shown by x symbols, but they were not considered in the calculations of the rotational temperatures. The vertical error bars are calculated from the uncertainties of the integrated fluxes (uncertainty from the Gaussian fitting plus 10% of the total flux from the calibration of the data) and are considered in the fitting process.

From the population diagram shown in Fig. 2, we find $T_{\rm rot} = 145 \pm 40$ K and $T_{\rm rot} = 320$ K for regions 1 and 2, respectively. The accuracy of the latter results is limited as we only have two points in the population diagram that correspond to rotational lines in $v = 0$. Using $Z(145\ {\rm K}) = 183.57$ and $Z(320\ {\rm K}) = 404.73$, we find mean column densities $N_{\rm AlF} = (3.6 \pm 1.1) \times 10^{15}$ cm^{-2} and $N_{\rm AlF} = 2.1 \times 10^{16}$ cm^{-2} for regions 1 and 2, respectively, as listed in Table 3 (Model A).

To test our assumption of optically thin emission, we estimated the optical depth at the line centre of all lines from all selected regions using

$$\tau_0 = \frac{c^2 A_{\rm ul} N_{\rm u}}{8\pi\nu^2 \Delta\nu \sqrt{\pi}/2\sqrt{\ln 2}} \left(\exp\left(\frac{h\nu}{k_{\rm B} T_{\rm exc}}\right) - 1\right). \tag{3}$$

We find optical depths in the 0.09–0.5 range in region 1 and 0.1–0.5 in region 2, confirming our assumptions of emission that is not optically thick. To investigate the accuracy of the excitation temperature and column density from the population diagram, we calculated the flux density (S_ν) of the lines using

$$S_\nu = N_{\rm AlF} (\pi r_{\rm e}^2) \frac{g_{\rm u} \exp\left(\frac{-E_{\rm u}}{k_{\rm B} T_{\rm rot}}\right)}{Z_{\rm rot}(T_{\rm rot})} \frac{A_{\rm ul} h\nu}{4\pi d^2}\ \phi_\nu, \tag{4}$$

where $\phi_\nu = \exp(-(\nu - \nu_0)^2/\Delta\nu^2)/(\Delta\nu\sqrt{\pi})$ is the line profile where $\Delta\nu = \nu_0 \Delta v/c$, and we assumed $\Delta v = 4$ km s$^{-1,}$ which fits the width of the observed AlF lines. Using the derived column densities and rotational temperatures from the population diagrams in Eq. (4) to reproduce the synthetic spectra in both regions, we significantly under-predicted the line strength of the vibrationally excited $v = 1$ line (see dashed blue lines in Fig. 3 for region 1 and upper panel of Fig. 4 for region 2). As can be seen, the derived temperature and column density only characterise the populations of the rotational levels, which also indicates the quasi-thermal excitation discussed above. This can be caused by different excitation mechanisms dominating the excitation of the $v = 0$ and $v = 1$ levels. The ground state excitation is most likely dominated by molecular collision, while the vibartionally excited state is mostly populated by the radiation from the central star and therefore require a higher excitation temperature. Hence, we considered excitation temperatures for the rotational levels, $T_{\rm rot}$, and vibrational states, $T_{\rm vib}$, which are independent. In this way, the number of molecules in a given v state and J level is given by

$$N_{v,J} = N_{\rm AlF} (\pi r_{\rm e}^2) \frac{g_{\rm J} \exp\left(\frac{-E_{\rm J}}{k_{\rm B} T_{\rm rot}}\right)}{Z_{\rm rot}(T_{\rm rot})} \frac{g_{\rm v} \exp\left(\frac{-E_{\rm v}}{k_{\rm B} T_{\rm vib}}\right)}{Z_{\rm vib}(T_{\rm vib})}, \tag{5}$$

where $g_J = (2J + 1)$ and $g_{\rm v} = 1$ are the rotational and vibrational degeneracy, E_J and E_ν are the rotational and vibrational excitation energies, and $Z_{\rm rot}$ and $Z_{\rm vib}$ are the rotational and vibrational partition functions and are given by

$$Z_{\rm rot}(T_{\rm rot}) = \sum_J (2J + 1) {\rm e}^{-J(J+1)B/k_{\rm B} T_{\rm rot}}, \tag{6}$$

where we considered that J runs from 0 to 94 and $B = 16488.355$ MHz, which is taken from CDMS (Yousefi & Bernath 2018).

$$Z_{\rm vib}(T_{\rm vib}) = \sum_{\rm v} e^{-E_{\rm v}/k_{\rm B} T_{\rm vib}}; \tag{7}$$

here, the vibrational state v runs from 0 to 5, which are the levels available in CDMS. We varied $N_{\rm AlF}$ and $T_{\rm vib}$ in Eq. (5) to obtain the best fit model to all observed lines in regions 1 and 2. We find that a vibrational temperature of $T_{\rm vib} = 1300 \pm 500$ K with associated $Z_{\rm vib} = 1.71$ and column densities of AlF molecules $N_{\rm AlF} = (5.8 \pm 2.0) \times 10^{15}$ cm^{-2} and $N_{\rm AlF} = (3.0 \pm 0.7) \times 10^{16}$ cm^{-2} reproduces the flux density of all observed line in regions 1 and 2, respectively (see dashed red lines in Figs. 3 and 4). These best models are selected based on a chi-square analysis and the results are summarised in Table 3 (Model C).

We note that if we include the $v = 1$ data point in the calculation of the excitation temperature and column density in the population diagram shown in Fig. 2, this results in an excitation temperature of $T_{\rm rot} = 1332 \pm 794$ K and a column density of $N_{\rm AlF} = (2.7 \pm 0.7) \times 10^{16}$ cm^{-2} for region 1. The derived temperature is in agreement with the vibrational temperature that we derived from separating the rotational and vibrational temperature above; however, the column density is higher by a factor of four assuming the same emitting region, which results in an overestimation of the flux density of all observed lines. For region 2, it results in $T_{\rm rot} = 956 \pm 100$ K and a column density of $N_{\rm AlF} = (7.5 \pm 0.4) \times 10^{16}$ cm^{-2} which also results to an overestimation of the flux density of observed lines (Model B in Table 3).

The AlF lines in region 3 are also not very optically thick, with optical depths at the line centre of 0.8 and 0.02 for $v = 0$ and 1 lines, respectively, calculated using Eq. (3). For region 3, we assumed the same rotational and vibrational temperatures of $T_{\rm rot} = 320$ K and $T_{\rm vib} = 1300 \pm 500$ K as we found in region 2. This results in an AlF column density of $N_{\rm AlF} = (5 \pm 2) \times 10^{16}$ cm^{-2}. The model results overlaid with the observed spectra are presented in the lower panel of Fig. 4. The summary of the derived column densities in all regions are listed in Table 3.

3.1.2. AlF/H$_2$ fractional abundance

Estimating the AlF/H$_2$ fractional abundance is subject to a relatively larger uncertainty because the gas density and temperature

Table 3. Results of excitation analysis of AlF towards *O* Ceti in three selected regions shown in Fig. 1.

Region	Diameter ($R_\star$)	$T_{\rm rot}$ (K)	$T_{\rm vib}$ (K)	$N_{\rm AlF/H_2}$ (cm^{-2})	$N_{\rm H_2}^{(*)}$ (cm^{-2})	$f_{\rm AlF/H_2}$	Model
1	22	145 ± 40	145 ± 40	$(3.6 \pm 1.1) \times 10^{15}$			A
1	22	1332 ± 794	1332 ± 794	$(2.7 \pm 0.7) \times 10^{16}$			B
1	22	145 ± 40	1300 ± 500	$(5.8 \pm 2.0) \times 10^{15}$	2.4×10^{23}	$(2.5 \pm 1.7) \times 10^{-8}$	C
2	11	320	320	2.1×10^{16}			A
2	11	956 ± 100	956 ± 100	$(7.5 \pm 0.4) \times 10^{16}$			B
2	11	320	1300 ± 500	$(3.0 \pm 0.7) \times 10^{16}$	2.0×10^{24}	$(1.5 \pm 0.8) \times 10^{-8}$	C
3	4	320	1300 ± 500	$(5.0 \pm 2.0) \times 10^{16}$	6.1×10^{24}	$(0.8 \pm 0.5) \times 10^{-8}$	C

Notes. For regions 1 and 2: models A include $\upsilon = 0$ lines in the population diagram (PD) to calculate the excitation temperature and column density which result to underestimation of the flux density of $\upsilon = 1$ lines as shown by blue dashed lines in Figs. 3 and 4, models B include both $\upsilon = 0$ and $\upsilon = 1$ lines in the PD, which results in the overestimation of the flux densities of all lines, and model C separates $T_{\rm rot}$ and $T_{\rm vib}$ and results in the best model outcomes, as shown in Figs. 3 and 4 with red and green dashed lines and discussed in Sect. 3.1.1. $^{(*)}$We note that $N_{\rm H_2}$ is uncertain by a factor of two, as discussed in Sect. 3.1.2.

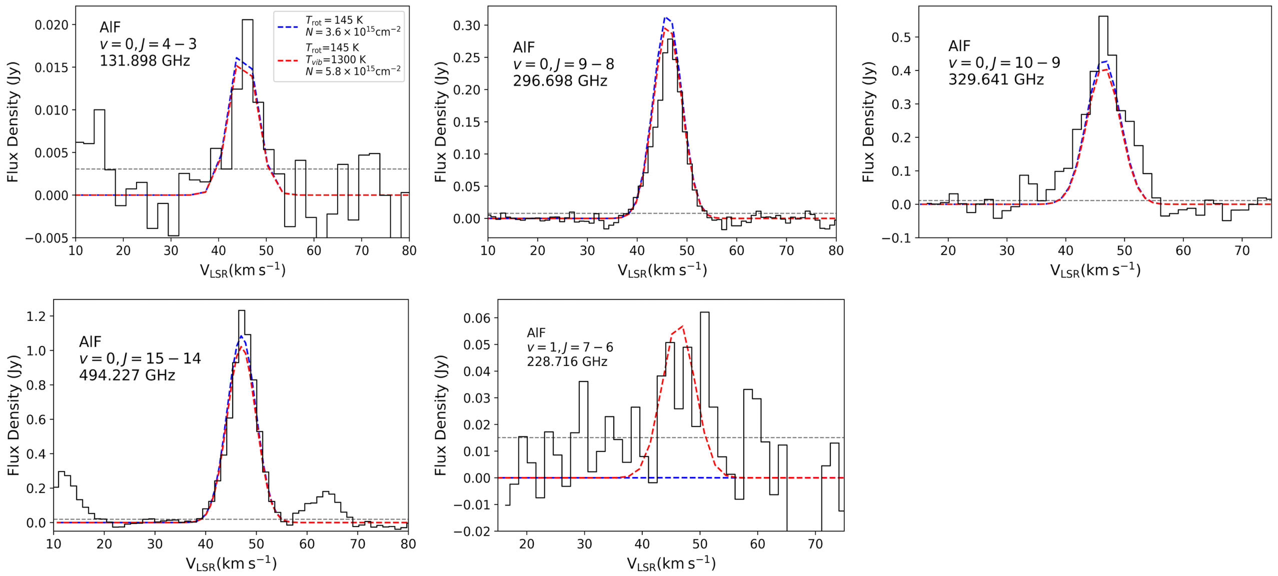

Fig. 3. AlF lines observed by ALMA towards *o* Ceti that are listed in Table 2 extracted from region 1 (black solid lines) overlaid with model results (dashed lines). Models indicate that two separate rotational and vibrational temperatures are need to reproduce all observed lines, which is discussed in Sect. 3.1. The line rest frequencies and transitions are marked in each panel. The grey dashed lines show the rms level.

distributions in the extended atmospheres and wind-acceleration regions is variable and complex with regard to time.

Moreover, Mira is in a binary system including Mira A (*o* Ceti) and a white dwarf (Mira B) at a distance of ∼0.5″ (Ramstedt et al. 2014). It is well known that the binary companion affects the gas density at large scales (5″−10″) Ramstedt et al. (2014). However, the gravitational field is expected to be dominated by Mira A up to ∼0.3″ ∼20 $R_\star$ in the inner most region Mohamed & Podsiadlowski (2012). Therefore, the binary companion is not expected to influence the gas density in the regions we study here.

The radiation field is likely strongly affected by Mira B in the UV spectral region, even close to Mira A as suggested by the relative UV brightness of the two sources reported by Karovska et al. (1997). This probably affects the molecular abundances in the inner CSE, but how the different parameters of binary systems influence the abundances of specific molecules is not yet established. This is a topic of ongoing research (e.g. Saberi et al. 2018, 2019; Van de Sande & Millar 2022). We speculate that the asymmetry seen in the AlF molecular distribution (*J* = 10–9) seen in Fig. 1 could be due to the gravitational influence of Mira B, but investigating this is beyond the scope of this paper.

To constraining the H_2 gas column density, we used the spatially resolved $C^{18}O(\upsilon = 0,\ J = 3–2)$ line observed with ALMA. We calculated the H_2 column density towards the three different regions described in Sect. 3.1.1. To convert the $C^{18}O$ column density to H_2 column density, we assumed the typically used CO fractional abundance $f_{\rm C^{16}O/H_2} = 4 \times 10^{-4}$ for M-type AGB stars (e.g. Khouri et al. 2018), and a ratio $^{16}O/^{18}O = 282 \pm 100$ reported for *o* Ceti by Hinkle et al. (2016). Together, these imply a fractional abundance of $C^{18}O$, $f_{\rm C^{18}O/H_2} = (1.4 \pm 0.6) \times 10^{-6}$.

For the excitation analysis of the $C^{18}O$ line, we used the RADEX[1] radiative transfer code. We considered a line width of 6 km s^{-1} and varied the excitation temperature and $C^{18}O$ column density to reproduce the observed $C^{18}O$ flux from observations.

---

[1] `http://var.sron.nl/radex/radex.php`

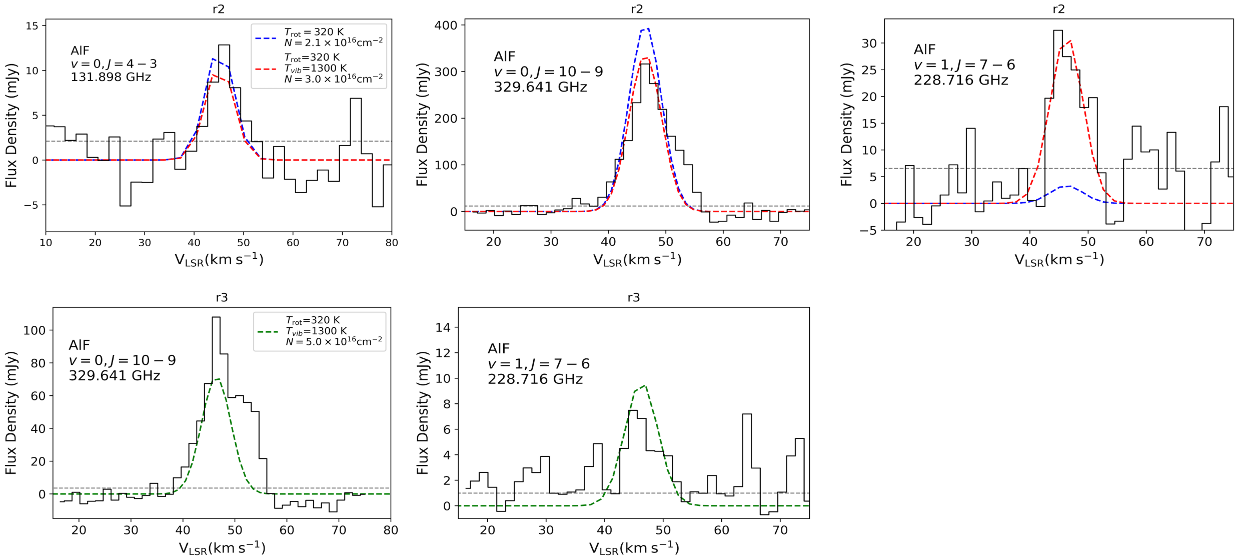

Fig. 4. AlF lines observed by ALMA towards *o* Ceti extracted from region 2 with a diameter of 0.168″ ∼11$R_\star$ (*upper panel*) and region 3 with diameter of 0.055″ × 0.07″ ∼4 $R_\star$ (*lower panel*) shown with black solid lines overlaid with model results (dashed lines). Models indicate that two separate rotational and vibrational temperatures are needed to reproduce all observed lines, which is discussed in Sect. 3.1. The line rest frequencies and transitions are marked in each panel. The grey dashed lines show the rms level. We note that the asymmetric feature in the right wing of the J = 10–9 line in region 3 might be due to a blend with a high excitation SO_2 line lying at 329.6459 GHz that becomes more prominent in the innermost regions of the circumstellar envelope.

Calculations of the H_2 gas density in the three selected regions are given below.

In region 1, the brightness temperature of the $C^{18}O$ line peaks at 13 K, corresponding to a flux density of 90 mJy as shown in Fig. A.1. We varied the $C^{18}O$ excitation temperature and column density for $C^{18}O$ to reproduce the observed flux density. Assuming an excitation temperature of 700 ± 300 K, we found that a column density $N_{C^{18}O} = (3.3 \pm 1.3) \times 10^{17}\,\mathrm{cm}^{-2}$ reproduces the observed line. Considering $f_{C^{18}O/H_2} = (1.4 \pm 0.6) \times 10^{-6}$ gives the H_2 column densities $N_{H_2} = 2.4 \times 10^{23}\,\mathrm{cm}^{-2}$. The derived N_{H_2} has an uncertainty of a factor of 2.1 considering the uncertainty on the $^{16}O/^{18}O$ isotopic ratio and excitation temperature. Assuming the AlF column density of $N_{AlF} = (5.8 \pm 2) \times 10^{15}\,\mathrm{cm}^{-2}$ that we describe in the previous section, we find an AlF fractional abundance of $f_{AlF/H_2} \sim (2.5 \pm 1.7) \times 10^{-8}$ in region 1.

In region 2, the brightness temperature of the $C^{18}O$ line peaks at 30 K, corresponding to a flux density of 55 mJy. Similarly to region 1, we varied the excitation temperature and the column density of $C^{18}O$ to reproduce the line flux extracted from region 2. We assumed an excitation temperature of 1500 ± 500 K and found a column density of $N_{C^{18}O} = (1.5 \pm 0.5) \times 10^{18}\,\mathrm{cm}^{-2}$ that reproduces the $C^{18}O$ line. These yield a H_2 column density of $N_{H_2} = 1.1 \times 10^{24}\,\mathrm{cm}^{-2}$ with an uncertainty of a factor of 1.8 due to the uncertainties on the isotopic ratio and the excitation temperature. For the same region, Khouri et al. (2018) reported $N_{H_2} = 3.4 \times 10^{24}\,\mathrm{cm}^{-2}$ based on the radiative transfer modelling of the CO (v = 1, J = 3–2) and ^{13}CO (v = 0, J = 3–2) line. Thus, a column density of $N_{H_2} \sim 2 \times 10^{24}$ would be consistent with both the value determined by us and those by Khouri et al. (2018) given the intrinsic uncertainties and different approaches, and is probably a better estimate of the real column density. The best model from Sect. 3.1.1 gave an AlF column density $N_{AlF} = (3.0 \pm 0.7) \times 10^{16}\,\mathrm{cm}^{-2}$. Therefore, the estimated H_2 and AlF column densities result to a fractional abundance of $f_{AlF/H_2} \sim (1.5 \pm 0.8) \times 10^{-8}$ in region 2.

In region 3, the $C^{18}O$ brightness temperature peaks at 160 K corresponding to a flux density of 38 mJy. We assumed an excitation temperature of 1500 ± 500 K and found a column density of $(8.5 \pm 2.5) \times 10^{18}\,\mathrm{cm}^{-2}$ for $C^{18}O$ to reproduce the observed brightness temperature in this region. This implies a H_2 column density of $N_{H_2} = 6.1 \times 10^{24}\,\mathrm{cm}^{-2}$ with an uncertainty of a factor of 2.0. From Sect. 3.1.1, we find an AlF column density of $N_{AlF} = (5 \pm 2) \times 10^{16}\,\mathrm{cm}^{-2}$ for the best model. These translate to a fractional abundance of $f_{AlF/H_2} \sim (0.8 \pm 0.5) \times 10^{-8,}$ and in region 3 this is within 4$R_\star$. The derived fractional abundances in the three regions are listed in Table 3 (Model C).

Our derived AlF fractional abundances in the three regions are consistent with chemical models of Agúndez et al. (2020, see Fig. A.4,) which also predict a mean AlF fractional abundance of $\sim 10^{-8}$ within $\sim 9R_\star$ and also a lower abundance in a range of $\sim 10^{-11}$–10^{-8} in the innermost region with a radius of $1R_\star < R < 3R_\star$. Considering the initial mass of *o* Ceti ∼1 $M_\odot$, our results are also in agreement with the stellar yield models by Lugaro et al. (2004); Karakas (2010) and are consistent with the Solar F budget of $F/H_2 = (5 \pm 2) \times 10^{-8}$ (Asplund et al. 2021).

3.1.3. The excitation of AlF

The derived rotational temperatures of 320 K and 145 K from the population diagram in the inner CSE are rather low and seem to indicate sub-thermal excitation of AlF. A detailed study of the excitation of AlF is necessary to understand the distribution of the level populations. However, such an analysis is complicated by the fact that the radiation field as a function of position is poorly constrained at the relevant wavelengths (because of, for example, dust absorption and emission). We do not expect the binary companion to have a significant effect on the radiation field close to Mira A at the relevant wavelengths.

Although, the three-dimensional gas density distribution in the inner region of *o* Ceti is only constrained by one-dimensional models. Nonetheless, we were able to estimate the relative effects of collisions and the radiation field on the excitation of AlF.

The radiative pumping of AlF from $\upsilon = 0$ to $\upsilon = 1$ takes place through an infrared band at 12.48 μm. Assuming the

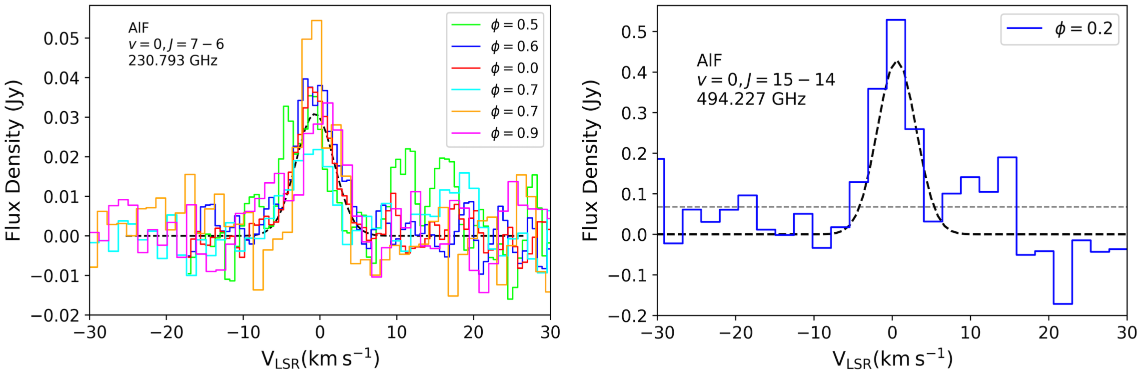

Fig. 5. ALMA observations of AlF line emission towards R Leo (solid lines) and the results of an LTE model (dashed black lines). Stellar variability phases (ϕ) are indicated in the upper-right, and the line transitions are indicated in the upper-left panels. The grey dashed lines show the rms level.

effective temperature and effective near-infrared (IR) radius as determined by Wittkowski et al. (2016), we can estimate the 12.48 µm flux density for a 2450 K black body, and we find a flux density of ~500 Jy. This does not include the contribution from diffuse emission from dust and the binary companion and, hence, is a lower limit to the actual radiation field. For comparison, this naked-star estimate corresponds to 0.23 times the flux taken directly from the infrared space observatory (ISO) observations[2].

To compute the mean intensity at 12.48 µm from a naked star with the considered radius and effective temperature, we calculated the dilution of the radiation field over the solid angle of region 1 ($\Omega = 2.134 \times 10^{-12}$ sr). We find a mean intensity of $J_\nu = F_\nu/\Omega = 1.04 \times 10^{-8}$ ergs s^{-1} cm^{-2} Hz^{-1} sr^{-1}. The IR pumping rate can be written as $\rho = A_{\rm vib}\, J_\nu/(2hc(\nu/c)^3) = 0.1\,{\rm s}^{-1}$, where $A_{\rm vib} \sim 8.62\,{\rm s}^{-1}$ is the spontaneous-emission coefficient of AlF for a v = 1–0 transition. Considering collisional rates of $\sim 2 \times 10^{-10}$ cm^3 s^{-1} (Danilovich et al. 2021), we find a upper limit for the H_2 densities below which IR pumping dominates by 10^9 cm^{-3}. If the radiation field is stronger than our naked-star estimate, the IR pumping will be efficient at larger densities. Given the observed ISO spectrum integrated over a much larger area than region 1, the mean intensity is likely at most a factor of a few larger than our estimate.

Assuming depths for regions 1 and 2 along the line of sight similar to their radial extent on the sky ($\sim 5 \times 10^{14}$ cm and $\sim 3 \times 10^{14}$ cm, respectively), the H_2 column densities we obtained imply average densities in these regions of $\sim 5 \times 10^8$ cm^{-3} and $\sim 4 \times 10^9$ cm^{-3}. Hence, the radiation field is expected to dominate the excitation through vibrational pumping in a large fraction of region 1 but not as much in region 2. Interestingly, IR pumping would be expected to help increase the rotational temperature of the v = 0 levels for low gas densities, making the low values we derive puzzling. In order to study the excitation of AlF in detail, radiative transfer models including the three-dimensional gas-density distribution and mean intensity at relevant frequencies is necessary. Nonetheless, the rotational and vibrational temperatures we derive provide an empirical description of the average excitation of AlF and can be used to infer column densities as above.

3.1.4. HF

As discussed in Sect. 1, HF is among the two most abundant F-bearing species in the outflow of AGB stars (Agúndez et al. 2020). We investigated the archive HF data available for *o* Ceti, aiming to determine the HF fractional abundance and the total F budget in the gas phase. There is a tentative detection of HF (J = 1–0) at 1232.476 GHz observed with Herschel/SPIRE. There is also potential detection of the HF lines (J = 2–1, 3–2, and 4–3) observed by PACS in Herschel. However, all these lines are blended with H_2O lines, making it difficult to determine the HF fractional abundance based on low spectral resolution of Herschel data.

3.2. R Leo

In R Leo, the AlF (v = 0, J = 7–6) line is detected at five different epochs with ALMA at various pulsation phases. The data are taken over a period of one year at a visual phase of ϕ = 0.0, 0.5, 0.6, 0.7, and 0.9. One extra line of AlF (v = 0, J = 15–14) is covered by the ACA observations. All the covered lines with their spectroscopic parameters and measured intensities are listed in Table 2. The observations show that the emission region is barely resolved by the ~0.13″ beam (Fig. B.1). The line flux extracted from the higher angular-resolution images (beam ~0.02″) increases up to apertures of ~0.25″. Hence, we considered the emission region to have a diameter of ~0.25″ ~33 au ~$18R_\star$.

Figure 5 presents the multi-epoch observations of AlF at 230.79 GHz. Our observations with the highest angular resolution at ϕ =0.7 and 0.9 are subject to flux loss due most likely to the limited maximum recoverable scale of 0.4–0.6″ shown in Fig. 5, left panel, with magenta and cyan profiles. The flux variation seen in the AlF (J = 7–6) line is most likely due to low surface brightness sensitivity of the long baseline observations and the added limitations related to imaging emission with an extent similar to the maximum recoverable scale. Possible small calibration uncertainties on the shortest baselines and changes in antenna configuration between the observations makes a direct comparison between the highest angular resolution observations uncertain. Therefore, based on the current observations, we cannot confirm any flux variation due to the stellar variability.

For the population diagram, we used the weighted mean value of the first three J = 7–6 data points that are listed in Table 2. We removed the three observations with MRS < 0.6″ that are likely subject to flux loss. As shown in Fig. 6, we derived the rotational temperature of $T_{\rm rot} \sim 300$ K and the column density of $N_{\rm AlF} \sim 3.0 \times 10^{15}$ cm^{-2}. The accuracy of the results is limited since we only have two points in the population

---

[2] `https://irsa.ipac.caltech.edu/data/SWS/`

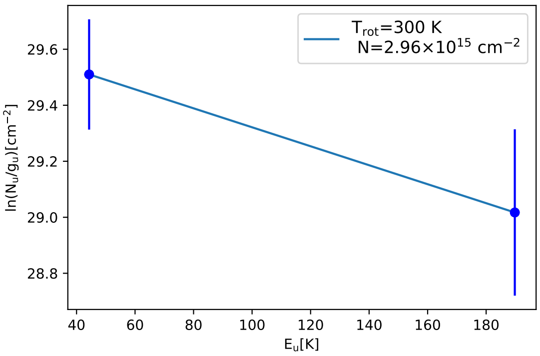

Fig. 6. Population diagram of observed AlF rotational lines towards R Leo. The data point with E_u = 44 K is the mean of the first three observations that are listed in Table 2 (see Sect. 3.2 for explanations).

diagram. We used the column density and the rotational temperature derived from the population diagram to reproduce the observations. The observed spectra and the model results are presented in Fig. 5.

Since R Leo and *o* Ceti have similar mass-loss rates and pulsation periods, we assumed the same H_2 column density of $(2.4 \pm 1.4) \times 10^{23}$ cm^{-2} as we derived for a region with a radius of 17 au in *o* Ceti (region 1). We also crudely estimated an AlF fractional abundance of $f_{AlF/H_2} \sim (1.2 \pm 0.5) \times 10^{-8}$ for R Leo.

3.3. R Dor, W Hya, and IK Tau

We report a tentative detection of AlF ($v = 0$, $J = 15$–14) line emission at 494.223 GHz towards W Hya and R Dor. We also report tentative detection of AlF ($v = 0$, $J = 7$–6) line emission at 230.79 GHz towards IK Tau and W Hya. The observed lines with their properties extracted from Gaussian fits are listed in Table 2. We assumed an emitting region of $11R_\star$, where $R_\star$ refers to the stellar radius measured in infrared as listed in Table 1, for these sources similar to what we derived from observations of *o* Ceti. This results in an emitting region with a radius of 22 au for W Hya, 13.5 au for R Dor, and 17.5 au for IK Tau.

We considered T_{rot} of 145 K from Mira region one and 300 K from Mira region two and R Leo to estimate the mean column density in these sources. The results are listed in Table 4. The model results overlaid on the observed spectra are presented in Fig. C.1.

To estimate the fractional abundances for these sources, we need to know the H_2 column density. Since AlF emission is compact and it comes from a region that can still be gravitationally bound to the star, part of the gas will be ejected and some will fall back to the star. Hence, estimating gas densities in these inner regions from extrapolating models obtained based on the large-scale envelope will lead to errors in the estimated gas densities. Moreover, densities from models for the large-scale envelopes are uncertain by a factor of a few Ramstedt et al. (2008). Finally, the way in which the densities in the extended atmosphere differ from those predicted by extrapolating the mass-loss rate inwards may vary between stars because of differences in the extended atmospheres and wind-acceleration region (e.g. Habing 1996; Höfner & Olofsson 2018).

To roughly estimate the AlF fractional abundances in these sources, we used the H_2 column density that we derived for *o* Ceti of $(2.4 \pm 1.4) \times 10^{23}$ cm^{-2} within a radius of $11R_\star$ from the central star. This suggests the AlF/H_2 fractional abundance is within a range of $\sim(0.1–4) \times 10^{-8}$ for these sources as listed in Table 4. This is in agreement with the Solar fractional abundance of F and the stellar yield models for AGB stars with initial masses in range of 1–2 $M_\odot$. We note that the approximation we made above is crude. This is even less certain for IK Tau and R Dor due to different mass-loss rates (in case of IK Tau) and pulsation periods (in both cases) with respect to *o* Ceti, which may cause even larger differences in the H_2 gas density and fractional abundances in the inner region. A proper determination of AlF abundances will require a study of gas densities in the AlF emission regions.

Table 4. Approximation of AlF column density and fractional abundance in other sources.

Star	T_{rot} = 145 (K)		T_{rot} = 300 (K)	
	N_{AlF} (cm^{-2})	f_{AlF/H_2}	N_{AlF} (cm^{-2})	f_{AlF/H_2}
R Leo			3×10^{15}	1.2×10^{-8}
R Dor	2.5×10^{14}	0.1×10^{-8}	3×10^{14}	0.12×10^{-8}
W Hya	1.2×10^{15}	0.5×10^{-8}	1.5×10^{15}	0.6×10^{-8}
IK Tau	0.6×10^{16}	2.5×10^{-8}	1×10^{16}	4.2×10^{-8}

Notes. For R Leo, the T_{rot} and N_{AlF} are estimated using the PD shown in Fig. 6. For other sources, we used T_{rot} estimated for *o* Ceti and R Leo to approximate N_{AlF}. For all sources, the H_2 density of 2.4×10^{23} cm^{-2} is used as derived for *o* Ceti.

4. Discussion and summary

The cosmic origin of F is still uncertain. AGB stars are among the few candidates to synthesis F in our Galaxy. From stellar yield models, the efficiency of F synthesis in AGB stars strongly depends on the initial mass and metallicity (Lugaro et al. 2004; Karakas 2010). For Solar metallicity, the F synthesis is maximal for stars with an initial mass of 2–4 $M_\odot$. From chemical models by Agúndez et al. (2020), a significant amount of F is expected to be locked into AlF and HF in the outflow of all chemical types of AGB stars. In this paper, we report the first detection of AlF line emission towards five oxygen-rich AGB stars observed with ALMA: *o* Ceti, R Leo, W Hya, R Dor, and IK Tau.

Towards *o* Ceti, we detected five rotational lines and determined the fractional abundance of $f_{AlF/H_2} \sim (0.8 \pm 0.5) \times 10^{-8}$ within a radius of $2R_\star$, $\sim(1.5 \pm 0.8) \times 10^{-8}$ within a radius of $5.5R_\star$, and $\sim(2.5 \pm 1.7) \times 10^{-8}$ within a radius of $11R_\star$ from population diagram analysis. The observations are best reproduced by considering independent rotational and vibrational excitation temperatures. These derived fractional abundances at various radii from the star are in agreement with f_{AlF/H_2} molecular distribution for an M-type AGB star from the recent chemical models by Agúndez et al. (2020). This indicates how spatially resolved observations of several transitions can verify the accuracy of chemical models on predictions of molecular fractional abundances as long as the H_2 gas density in the emitting region is known.

Towards R Leo, we find a column density of 3×10^{15} cm^{-2} for an emission region with radius $\sim 9\,R_\star$. For other sources, we considered the rotational temperatures of 145 K and 300 K as derived for *o* Ceti and R Leo to make a rough estimation of the AlF column density. These result in $N_{AlF} \sim (1.2$–$1.5) \times 10^{15}$ cm^{-2} in W Hya, $\sim(2.5$–$3.0) \times 10^{14}$ cm^{-2} in R Dor, and $\sim(0.6$–$1.0) \times 10^{16}$ cm^{-2} in IK Tau within a radius of $11R_\star$ from central stars. However, spatially resolved observations towards these sources are necessary to resolve the line emitting regions and constrain the column densities. By assuming the same H_2 column density as we derived for *o* Ceti, we can make a crude approximation of the AlF fractional abundance $(1.2 \pm 0.5) \times 10^{-8}$ in R Leo and in a range of $(0.1–4) \times 10^{-8}$ for W Hya, R Dor, and IK Tau.

All observed sources in our sample have an initial mass in the range of $M \sim 1–2\,M_\odot$ and are Galactic sources with metallicities probably similar to solar; thus, they are not expected to efficiently synthesise fluorine from stellar yield models by Lugaro et al. (2004); Karakas (2010). Our results for all sources are in a good agreement with both stellar yield models and chemical models.

Danilovich et al. (2021) recently reported the detection of AlF and HF towards the S-type AGB star, W Aql. Using radiative transfer analysis, they found fractional abundances of $f_{\mathrm{AlF/H_2}} = 1 \times 10^{-7}$ and $f_{\mathrm{HF/H_2}} = 1 \times 10^{-8}$. Their reported value in the inner part is a higher than expected AlF abundance for W Aql, which has an initial mass within a range of $1.2–1.6\,M_\odot$ reported by De Nutte et al. (2017). This can indicate that either the mass of W Aql is larger, or that models for fluorine production predict nucleosynthesis at initial masses that are too large. However, the uncertainty in the radiative transfer analysis based on a single line observation and uncertainties in the physical parameters in the inner CSEs can play an important role in the molecular excitation analysis and abundance derivation.

The estimated $f_{\mathrm{AlF/H_2}}$ in all M-type AGB stars in our sample are in agreement with the reported $f_{\mathrm{AlF/H_2}}$ in the Sun and the C-type AGB star, IRC+10216, reported by Asplund et al. (2021) and Agúndez et al. (2012), respectively. We note that dependency of the AlF abundance on the AGB chemical type is not observationally constrained. This is due to very few observations that have been done so far to measure the abundances of F-bearing species in the outflow of evolved stars due to the lack of sensitivity of previous generations of observational facilities. Chemical models by Agúndez et al. (2020) have assumed the same photospheric abundance of $f_{\mathrm{AlF/H_2}} \sim 10^{-8}$ for M-, S-, and C-type AGB stars. Further observations in a larger sample from all chemical types are still needed to verify this assumption and also quantify the total F budget in various chemical types.

From chemical models, a significant overabundance of F due to stellar nucleosynthesis is expected to be seen in both AlF and HF abundances (M. Agúndez, priv. comm.). We remind the reader that the low spectral resolution of Herschel PACS/SPIRE data of HF observations make it impossible to distinguish the HF lines from the H_2O lines that are abundant in M-type AGB stars. Therefore, our study suggests that observations of AlF lines towards AGB stars with initial masses of $2–4\,M_\odot$ can provide more reliable observational evidence of the F nucleosynthesis predicted by stellar yield models of AGB stars. This is important with regard to understanding the role of AGB stars in the total F production in our Galaxy.

Acknowledgements. We thank John Black for fruitful discussions on the excitation of the AlF and all his comments on the manuscript. This paper makes use of the following ALMA data: ADS/JAO.ALMA#2016.1.00004.S, #2017.1.00191.S, #2018.1.00749.S, #2018.1.00649.S, #2016.1.01202.S, #2017.1.00862.S, #2016.1.00119.S, #2018.1.01440.S, and #2016.2.00025.S. ALMA is a partnership of ESO (representing its member states), NSF (USA) and NINS (Japan), together with NRC (Canada), MOST and ASIAA (Taiwan), and KASI (Republic of Korea), in cooperation with the Republic of Chile. The Joint ALMA Observatory is operated by ESO, AUI/NRAO and NAOJ. MS and SW acknowledge support by the SolarALMA project, which has received funding from the European Research Council (ERC) under the European Union's Horizon 2020 research and innovation programme (Grant agreement No. 682462), and by the Research Council of Norway through its Centres of Excellence scheme, project number 262622. TK, LVP and WV acknowledge support from the Swedish Research Council under grants No. 2019-03777 and 2014-05713. LVP acknowledges the ERC consolidator grant 614264. JPF has received funding support from the European Research Council under the European Union's Seventh Framework Program (FP/2007-2013)/ERC Grant Agreement No. 610256 NANOCOSMOS.

References

Abia, C., Recio-Blanco, A., de Laverny, P., et al. 2009, ApJ, 694, 971
Abia, C., Cunha, K., Cristallo, S., et al. 2010, ApJ, 715, L94
Abia, C., Cunha, K., Cristallo, S., & de Laverny, P. 2015, A&A, 581, A88
Abia, C., Cristallo, S., Cunha, K., de Laverny, P., & Smith, V. V. 2019, A&A, 625, A40
Agúndez, M., Cernicharo, J., Waters, L. B. F. M., et al. 2011, A&A, 533, L6
Agúndez, M., Fonfría, J. P., Cernicharo, J., et al. 2012, A&A, 543, A48
Agúndez, M., Martínez, J. I., de Andres, P. L., Cernicharo, J., & Martín-Gago, J. A. 2020, A&A, 637, A59
Asplund, M., Amarsi, A. M., & Grevesse, N. 2021, A&A, 653, A141
Danilovich, T., Lombaert, R., Decin, L., et al. 2017, A&A, 602, A14
Danilovich, T., Van de Sande, M., Plane, J. M. C., et al. 2021, A&A, 655, A80
De Nutte, R., Decin, L., Olofsson, H., et al. 2017, A&A, 600, A71
Federman, S. R., Sheffer, Y., Lambert, D. L., & Smith, V. V. 2005, ApJ, 619, 884
Fonfría, J. P., Santander-García, M., Cernicharo, J., et al. 2019, A&A, 622, L14
Francis, L., Johnstone, D., Herczeg, G., Hunter, T. R., & Harsono, D. 2020, AJ, 160, 270
Goldsmith, P. F., & Langer, W. D. 1999, ApJ, 517, 209
Grisoni, V., Romano, D., Spitoni, E., et al. 2020, MNRAS, 498, 1252
Habing, H. J. 1996, A&Ar, 7, 97
Hinkle, K. H., Lebzelter, T., & Straniero, O. 2016, ApJ, 825, 38
Hoeft, J., Lovas, F. J., Tiemann, E., & Törring, T. 1970, Zeit. Naturf. A, 25, 1029
Höfner, S., & Olofsson, H. 2018, A&Ar, 26, 1
Jönsson, H., Ryde, N., Spitoni, E., et al. 2017, ApJ, 835, 50
Jorissen, A., Smith, V. V., & Lambert, D. L. 1992, A&A, 261, 164
Karakas, A. I. 2010, MNRAS, 403, 1413
Karovska, M., Hack, W., Raymond, J., & Guinan, E. 1997, ApJ, 482, L175
Khouri, T., Vlemmings, W. H. T., Olofsson, H., et al. 2018, A&A, 620, A75
Limongi, M., & Chieffi, A. 2018, ApJS, 237, 13
Longland, R., Lorén-Aguilar, P., José, J., et al. 2011, ApJ, 737, L34
Lugaro, M., Ugalde, C., Karakas, A. I., et al. 2004, ApJ, 615, 934
McMullin, J. P., Waters, B., Schiebel, D., Young, W., & Golap, K. 2007, in Astronomical Data Analysis Software and Systems XVI, eds. R. A. Shaw, F. Hill, & D. J. Bell, Astronomical Society of the Pacific Conference Series, 376, 127
Meynet, G., & Arnould, M. 2000, A&A, 355, 176
Mohamed, S., & Podsiadlowski, P. 2012, Baltic Astron., 21, 88
Müller, H. S. P., Thorwirth, S., Roth, D. A., & Winnewisser, G. 2001, A&A, 370, L49
Müller, H. S. P., Schlöder, F., Stutzki, J., & Winnewisser, G. 2005, J. Mol. Struct., 742, 215
Olive, K. A., & Vangioni, E. 2019, MNRAS, 490, 4307
Pickett, H. M., Poynter, R. L., Cohen, E. A., et al. 1998, J. Quant. Spec. Radiat. Transf., 60, 883
Ramstedt, S., Schöier, F. L., Olofsson, H., & Lundgren, A. A. 2008, A&A, 487, 645
Ramstedt, S., Mohamed, S., Vlemmings, W. H. T., et al. 2014, A&A, 570, L14
Ryde, N., Jönsson, H., Mace, G., et al. 2020, ApJ, 893, 37
Saberi, M., Vlemmings, W. H. T., De Beck, E., Montez, R., & Ramstedt, S. 2018, A&A, 612, L11
Saberi, M., Vlemmings, W., Millar, T., & De Beck, E. 2019, IAU Sympos., 343, 191
Spitoni, E., Matteucci, F., Jönsson, H., Ryde, N., & Romano, D. 2018, A&A, 612, A16
Timmes, F. X., Woosley, S. E., & Weaver, T. A. 1995, ApJS, 98, 617
Van de Sande, M., & Millar, T. J. 2022, MNRAS, 510, 1204
Velilla Prieto, L., Sánchez Contreras, C., Cernicharo, J., et al. 2017, A&A, 597, A25
Vlemmings, W. H. T., Khouri, T., & Olofsson, H. 2019, A&A, 626, A81
Werner, K., Rauch, T., & Kruk, J. W. 2005, A&A, 433, 641
Wittkowski, M., Chiavassa, A., Freytag, B., et al. 2016, A&A, 587, A12
Woosley, S. E., & Weaver, T. A. 1995, ApJS, 101, 181
Wyse, F. C., Gordy, W., & Pearson, E. F. 1970, J. Chem. Phys., 52, 3887
Yousefi, M., & Bernath, P. F. 2018, ApJS, 237, 8
Ziurys, L. M., Apponi, A. J., & Phillips, T. G. 1994, ApJ, 433, 729

Appendix A: CO observation towards *o* Ceti

Figure A.1 presents $C^{18}O$ ($v = 0, J = 3-2$) line spectra extracted in region one towards *o* Ceti. The line has been used to estimate the H_2 gas density in region 1 as detailed in Sect. 3.1.2.

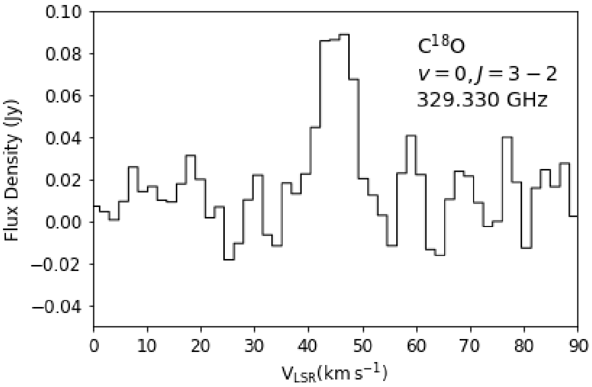

Fig. A.1. ALMA observations of $C^{18}O$ line towards *o* Ceti from region one. This line has been used for the estimation of H_2 density in region one as discussed in Sect. 3.1.2.

Appendix B: R Leo

Figure B.1 presents the integrated emission of the AlF ($J = 7-6$) line observed with a 0.133″ beam towards R Leo that is discussed in Section 3.2 as an estimator of the size of the emitting region.

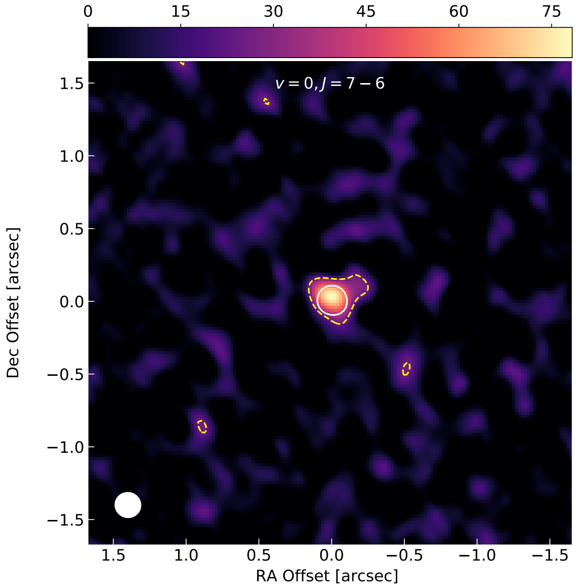

Fig. B.1. Integrated emission of AlF ($J = 7-6$) line towards R Leo. The lines are integrated in a range of -7 to 5 km/s. The scale is given in Jy km/s/beam. The white contours show the 50% stellar continuum emission level at the corresponding frequencies, and the dashed yellow contours mark the 3-σ level of the line emission. The filled white ellipses indicate the beam size (0.133″) in each observation.

Appendix C: R Dor, W Hya, and IK Tau

Figure C.1 presents the observed spectra for R Dor, W Hya, and IK Tau overlaid with the model results from Section 3.3.

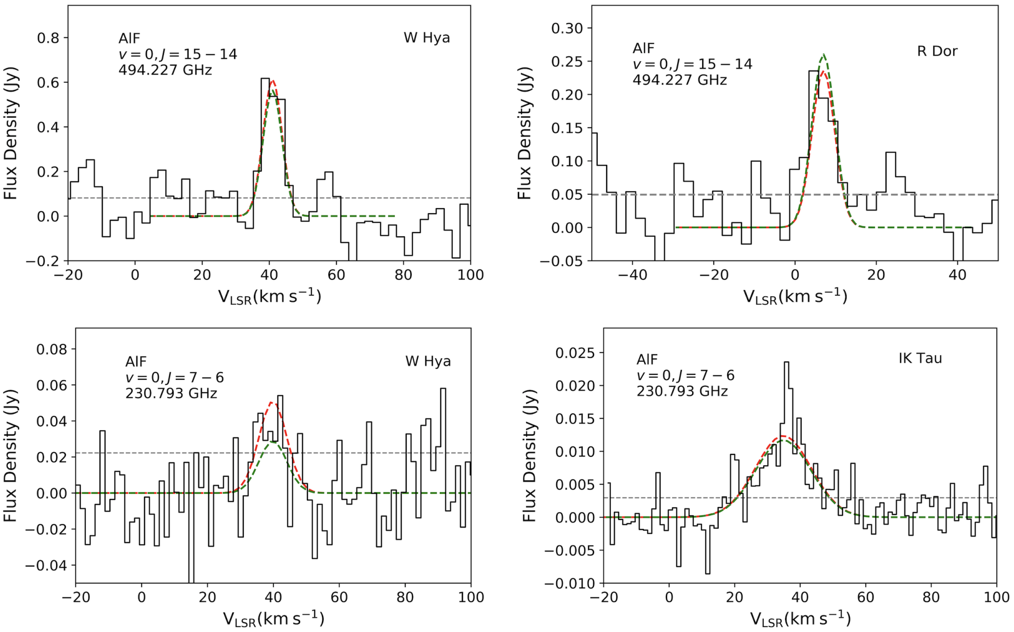

Fig. C.1. ALMA observations of AlF lines towards IK Tau, R Dor, and W Hya (Black solid lines) overlaid with LTE model results using $T_{\rm rot}$ = 145 K (red dashed lines) and $T_{\rm rot}$ = 300 K (green dashed lines) that are detailed in Sect. 3.3. The line rest frequencies and transition are stated in each panel. The AlF ($v=0$, $J=7$–6) line emission at 230.7938 GHz can potentially be blended with ^{50}TiO$_2$ line at 230.7931 GHz. The grey dashed lines show the rms level.